NAVAL POSTGRADUATE SCHOOL

MONTEREY, CALIFORNIA

THESIS

DESIGN AND SIMULATION OF A TERAHERTZ SENSOR USING FINITE ELEMENT MODELING

by

Poyuan Liao

December 2009

Thesis Advisor:	Gamani Karunasiri
Co-Advisor:	Dragoslav Grbovic

Approved for public release; distribution is unlimited

REPORT DOCUMENTATION PAGE		*Form Approved OMB No. 0704-0188*

Public reporting burden for this collection of information is estimated to average 1 hour per response, including the time for reviewing instruction, searching existing data sources, gathering and maintaining the data needed, and completing and reviewing the collection of information. Send comments regarding this burden estimate or any other aspect of this collection of information, including suggestions for reducing this burden, to Washington headquarters Services, Directorate for Information Operations and Reports, 1215 Jefferson Davis Highway, Suite 1204, Arlington, VA 22202-4302, and to the Office of Management and Budget, Paperwork Reduction Project (0704-0188) Washington DC 20503.

1. AGENCY USE ONLY *(Leave blank)*	2. REPORT DATE December 2009	3. REPORT TYPE AND DATES COVERED Master's Thesis	
4. TITLE AND SUBTITLE Designing and Simulating a Terahertz Sensor Using Finite Element Modeling		**5. FUNDING NUMBERS**	
6. AUTHOR(S) Poyuan Liao			
7. PERFORMING ORGANIZATION NAME(S) AND ADDRESS(ES) Naval Postgraduate School Monterey, CA 93943-5000		**8. PERFORMING ORGANIZATION REPORT NUMBER**	
9. SPONSORING /MONITORING AGENCY NAME(S) AND ADDRESS(ES) N/A		**10. SPONSORING/MONITORING AGENCY REPORT NUMBER**	

11. SUPPLEMENTARY NOTES The views expressed in this thesis are those of the author and do not reflect the official policy or position of the Department of Defense or the U.S. Government.

12a. DISTRIBUTION / AVAILABILITY STATEMENT Approved for public release; distribution is unlimited	12b. DISTRIBUTION CODE

13. ABSTRACT (maximum 200 words)
This thesis presents the theoretical modeling of a terahertz (THz) sensor based on a flexible bi-material cantilever that performs thermal deformation under THz illumination. This thermal deformation was induced by the large mismatch thermal expansion coefficient of two materials. As THz radiation illuminated on the absorber plat, the temperature of the structure increased, causing the cantilever to deflect. The magnitude of the deflection can be measured electronically or optically, which gives a measurement of the input THz signal. The bi-material structure in this thesis is composed of a silicon dioxide cantilever beam, with regions coated with aluminum. The effect of thickness of two layers on the bending, response time, signal-to-noise ratio will be discussed. Maximum bending angle can be found in the results from the example of silicon dioxide with thickness layer from 700nm to 1400nm. The imbalanced stress due to fabrication process was taken into account to compare with simulation results to provide a better assumption on thickness selection.

14. SUBJECT TERMS THz, terahertz, bi-material, micro-cantilever, microbolometer, QCL, quantum cascade laser, MEMS, detection, focal plane array, NETD			15. NUMBER OF PAGES 53
			16. PRICE CODE
17. SECURITY CLASSIFICATION OF REPORT Unclassified	18. SECURITY CLASSIFICATION OF THIS PAGE Unclassified	19. SECURITY CLASSIFICATION OF ABSTRACT Unclassified	20. LIMITATION OF ABSTRACT UU

THIS PAGE INTENTIONALLY LEFT BLANK

DESIGN AND SIMULATION OF A TERAHERTZ SENSOR USING FINITE ELEMENT MODELING

Poyuan Liao
Captain, Army, Republic of China (Taiwan)
Chung-Cheng Institute of Technology, 2002

Submitted in partial fulfillment of the
requirements for the degree of

MASTER OF SCIENCE IN APPLIED PHYSICS

from the

NAVAL POSTGRADUATE SCHOOL
December 2009

Author: Poyuan Liao

Approved by: Gamani Karunasiri
                 Thesis Advisor

                 Dragoslav Grbovic
                 Co-Advisor

                 Andres Larraza
                 Chairman, Department of Physics

THIS PAGE INTENTIONALLY LEFT BLANK

ABSTRACT

This thesis presents the theoretical modeling of a terahertz (THz) sensor based on a flexible bi-material cantilever that performs thermal deformation under THz illumination. This thermal deformation was induced by the large mismatch thermal expansion coefficient of two materials. As THz radiation illuminated on the absorber plate, the temperature of the structure increased, causing the cantilever to deflect. The magnitude of the deflection can be measured electronically or optically, which gives a measurement of the input THz signal. The bi-material structure in this thesis is composed of a silicon dioxide cantilever beam, with regions coated with aluminum. The effect of thickness of two layers on the bending, response time, signal-to-noise ratio will be discussed. Maximum bending angle can be found in the results from the example of silicon dioxide with thickness layer from 700nm to 1400nm. The imbalanced stress due to fabrication process was taken into account to compare with simulation results to provide a better assumption on thickness selection.

THIS PAGE INTENTIONALLY LEFT BLANK

TABLE OF CONTENTS

THIS PAGE INTENTIONALLY LEFT BLANK

LIST OF FIGURES

THIS PAGE INTENTIONALLY LEFT BLANK

LIST OF TABLES

THIS PAGE INTENTIONALLY LEFT BLANK

ACKNOWLEDGMENTS

Professor Gamani Karunasiri – my thesis advisor

Dr. Dragoslav Grbovic – my thesis co-advisor

THIS PAGE INTENTIONALLY LEFT BLANK

I.   INTRODUCTION

A.   BACKGROUND

In recent years, research has been rapidly developing in the terahertz (THz) frequency range. Due to its non-invasive properties, terahertz radiation has great potential in several areas of application such as inspection of fragile artwork, identification of concealed weapons, quality control in manufacturing, and medical imaging.

Detection of THz radiation has been investigated and reported in scientific literature [1]. The sensing of THz radiation by the photonic detector techniques normally requires a cryogenic operating temperature to reduce thermal noise. The imaging system includes a vacuum jacket to produce low pressure and a cooling system, making it relatively expensive.

To overcome this problem, the potential use of un-cooled infrared microbolometer camera technology for the THz detection has been investigated [2]. The camera's original focusing optics were replaced with a Tsurupica-based lens and the milliwatt-scale quantum cascade laser (QCL) was used as an illuminator. With this change, the camera was able to image frequencies down to 0.7 THz. One of the drawbacks of microbolometer technology is the generation of heat (self-heating) during readout, which limits the integration time to improve the signal-to-noise ratio [2]. In addition, microbolometer based focal plane arrays require integrated electronics for readout, making them relatively difficult to fabricate.

An alternative approach that eliminates self-heating as well as integrated readout electronics is detection based on the deflection of bi-material cantilever structures in response to thermal radiation [3, 4]. The amount of deflection can be readout using an external light source. These sensors can be easily fabricated using micro-electromechanical systems (MEMS) fabrication technologies. The bi-material micromechanical sensor under consideration is based upon a deformed micro-structure cantilever under THz illumination. The deformation is caused by different rates of

1

expansion due to the difference in thermal expansion coefficients of the two materials. Compared to the photon detectors, the bi-material un-cooled thermal detector has lower cost and is much more portable. However, the relatively long thermal time constant associated with high thermal isolation needed slow results in long response times. It is estimated that for real time imaging (30 frames per second), the thermal time constant needs to be less than 15 ms. The main focus of this thesis is to optimize the layer thickness of thin films used for fabricating the cantilever structure to achieve high sensitivity.

B.   BI-MATERIAL CANTILEVER SENSOR

The bi-material cantilever deforms by absorbing THz radiation by the absorption plate (see Figure 1), thereby causing a temperature increase in both materials. Since the top material has a higher thermal expansion coefficient than the bottom material, the cantilever tends to deform as depicted in Figure 1 [3]. The magnitude of the deflection is then measured electrically or optically and gives a measurement of the input signal.

Figure 1.   Deformation of bi-material cantilever (After: [3])

The readout system can be either electronic (capacitive or resistive), or optical. Electronic readout has been the most commonly used approach, mainly in microbolometers. However, as mentioned earlier it has several disadvantages. The main problem is its limited integration time due to self-heating. The electronic readout system with a large number of pixels requires complex circuitry that will make the

microfabrication process very complex and expensive. It will also make it very difficult to scale the arrays to high resolution. Compared to the electrical readout system, the optical readout is completely external and does not need any electrical leads attached to the sensor. This allows the use of low thermal conductivity material, which provides higher thermal isolation for achieving greater sensitivity. With this advantage, the optical readout becomes more desirable for bi-material based focal plane arrays (FPAs).

Figure 2 shows the schematic diagram of an optical readout system [4]. The incident THz radiation from the target source illuminates the backside of the FPAs housed in a vacuum chamber. The absorbed radiation creates an increase in temperature resulting in a subsequent deformation of the micro-cantilever pixels in the array. On the other hand, a visible light source from an LED illuminates the front side of the FPA. The light reflected from the FPA creates a thermal image and is recorded by a CCD camera.
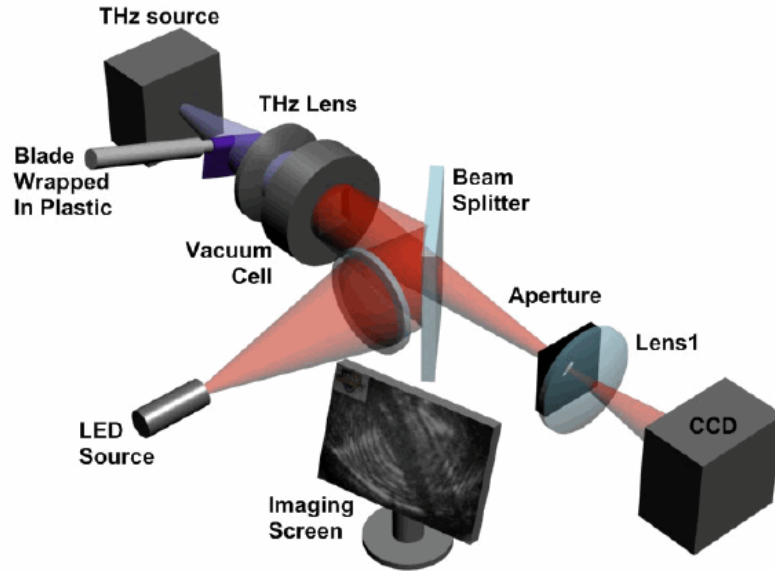

Figure 2.   Schematic diagram of an optical readout system (From: [4])

As previously discussed, the main physical property of the bi-material cantilever is a large difference in thermal expansion coefficients to obtain maximum deflection and achieve the operational goal. Clearly, the absorbing material needs to have the proper

absorption coefficient to ensure the desired wavelengths are captured. The physical properties of some of the most commonly used materials available in MEMS technology for bi-material thermal detectors are shown in Table 1 [3, 5, 6].

Table 1.   Properties of MEMS compatible materials suitable for bi-material sensor fabrication

	Thermal expansion coefficient $\alpha(x10^{-6}K^{-1})$	Thermal conductivity $g(Wm^{-1}K^{-1})$	Heat capacity $c(J\,kg^{-1}K^{-1})$	Emissivity ε
SiNx	2.1	19	691	0.8
SiO$_2$	0.4	1.4	730	0.8
Au	14.2	296	129	0.02
Al	25	237	900	0.02

As listed in Table 1, SiO$_2$ and Al have the lowest and highest thermal expansion coefficients, respectively. Comparing physical properties, these materials provide the largest difference in thermal expansion coefficients and hence provide maximum deflection of the cantilevers. Having a low thermal conductivity, SiO$_2$ provides the highest thermal isolation, which makes it perfect for use as the structural material for the sensor.

In the past, there have been difficulties in using SiO$_2$ as a MEMS structural layer due to the lack of a proper sacrificial layer in the micro-fabrication process [3]. As an alternative, SiNx was used in combination with Au or Al and became a more popular choice of materials for bi-material cantilever structures [3].

The SiO$_2$ based thermal detectors can now be produced using a new fabrication process without the use of a sacrificial layer, as reported by Dong et al [7] and as discussed in a previous thesis work [3]. Compared to SiNx, overall deflection improvement using SiO$_2$ was predicted to be 70% [3]. However, the high stress of SiO$_2$ creates an extra curvature that affects the reflected LED light signal. This additional curvature will remain a challenge but will be discussed in more detail in Chapter IV.

II. SENSOR DESIGN AND MODELING

The structure of the micro-cantilever in this thesis was based on a previous design that has been widely used for infrared detectors [8]. The two symmetrical pairs of folded legs hold the absorber, which also serves as the reflector for the readout light beam, and is located at the center of the detector as shown in Figure 3 [6]. Such configuration facilitates the magnification of individual deformations. The total deflection angle of the reflector can be calculated as the sum of the individual angles produced on the folded legs, i.e. $\theta = \theta_1 + \theta_2$.
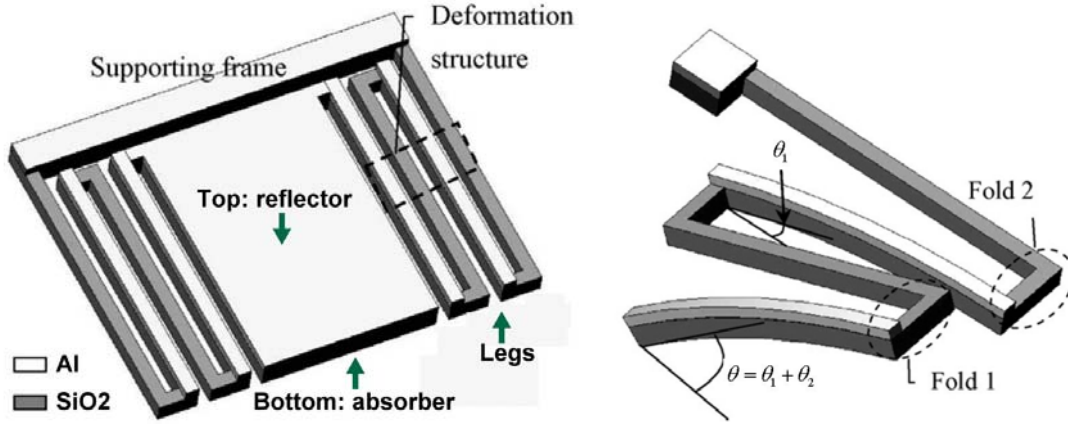

Figure 3.   The geometry of micro-cantilever with deflection amplification (After: [6])

In order to avoid diffraction effects, the size of the individual detectors (pixel) has to be larger than the wavelength of incoming radiation that is to be detected. In this thesis design, the measurement of one pixel is $200\mu m \, x \, 200\mu m$, which is capable of diffracting limited detection incident light from 2 THz ($150\mu m$) and upward. Another consideration of the structure design was the problems associated with partial device release due to the imperfections of the etching process. The release involves removal of the substrate from the back side using the Bosch etching process [9]. The Bosch process consists of two steps: polymer deposition and reactive etching (RIE). As shown below in Figure 4 [9], during the RIE step, silicon was removed rapidly by the ion bombardment gas. To

prevent extensive undercut during RIE (see Figure 4b), repeated polymer deposition steps are included to protect the sidewalls as depicted in Figure 4.

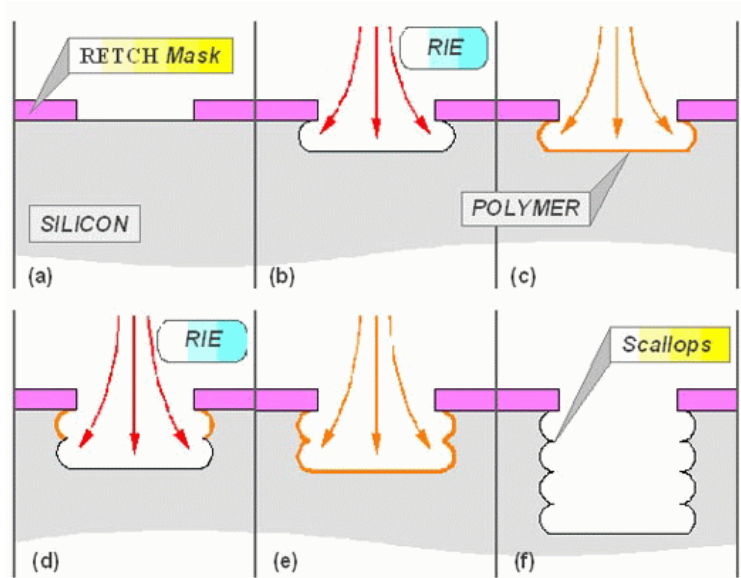Figure 4.   The steps of Bosch process where the undercut is minimized using a thin polymer layer (From: [9])

This process can result in discrepancies between the shape of the mask of the opening on one end of the wafer (see Figure 5a) and the actual opening of the mask after it reaches the opposite end, as illustrated in Figure 5b. Therefore, the design had to be adjusted to account for imperfections in the process.

<div align="center">(a)   (b)</div>

Figure 5.　　The over and under etch of different sections during substrate removal to isolate pixel

To overcome this problem, the pixel geometry had to be redesigned while taking into consideration the benefits of over etching. In this thesis, instead of having the same length of legs in a square area as in Figure 6a, a shorter and outward pair of legs outside the pixel was used to preserve extra space for over cutting as shown in Figure 6b. Figure 7 shows the detailed dimensions of the detector designed by Dr. Dragoslav Grbovic.

Figure 6.　　(a) Top view of initial design and (b) top view of new design to reduce over etching complete release

Figure 7.   Dimensions of the new pixel design

A.   PERFORMANCE ANALYSIS

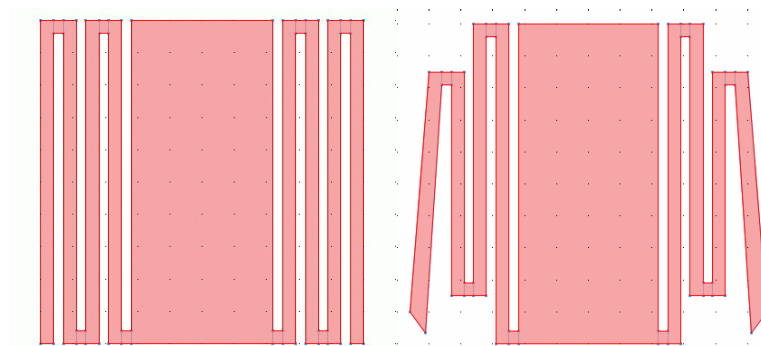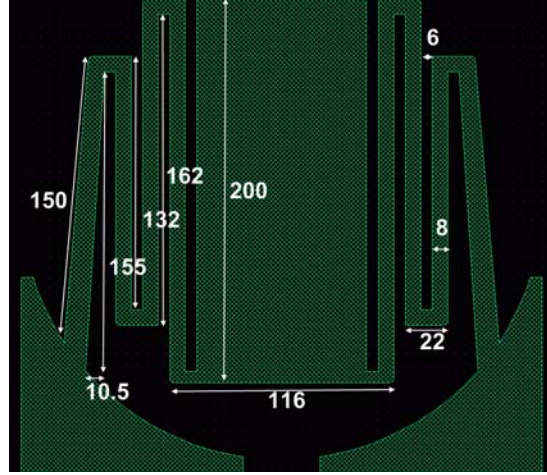The goal of this research is to improve the performance of the bi-material pixel. The performance is described by several parameters. The first parameter is the per-Kelvin deflection angle of cantilever where larger deflection angle corresponds to higher sensitivity. Therefore, a better performance can be expected due to the signal's being stronger than the surrounding noise. The second parameter is the thermal time constant. This describes how fast the detector is. The heated material must cool down to have the cantilever return to its original position and be ready for the next operational cycle. This process will take some amount of time, which will limit the speed at which the detector can be operated. The smaller the relaxation time, the faster detector operation can be. Therefore, the goal of this research is to maximize the per-Kelvin deflection angle and minimize the thermal time constant (response time).

To maximize the bending angle due to the given incoming power, the pixel needs to have a large increase in temperature, ΔT, as given by the following equation [3]:

$$\Delta T = \frac{P}{G} \tag{2.1}$$

Where P is total absorbed power (watts) and G is thermal conductance ($W \cdot K^{-1}$), which is the ability of material to conduct heat. For the same amount of absorbed power, the lower the value of G (value and based on the material and geometry), the higher the temperature change and hence larger the deflection angle.

Thermal conductance also has a great effect on the heat conduction. It is inversely proportional to the thermal response time. For the selected material with a heat capacity C ($J \cdot K^{-1}$), the higher the thermal conductance G, the smaller (faster) the device's heat dispersion time. The response time τ is determined by [3]:

$$\tau = \frac{C}{G} \tag{2.2}$$

As discussed above, the performance of the bi-material device is highly dependent on the thermal conductance of the device. The thermal conductance depends on the structure geometry design and the materials used. The major challenge in the design of the detector is the simultaneous optimization of both the bending angle and the response time. In order to maintain simplicity of processing, previous cantilever based infrared sensor research [3] provided a starting point for the present work. The detailed dimensions of the structure are listed in Table 2.

Table 2.   Structure dimensions used in the analysis

Pixel size (μm^2)	Absorber size (μm^2)	width of legs (μm)	length of legs (μm)
200×200	88×200	8	see Figure 7

B. THERMAL CONDUCTANCE AND ITS LIMIT

The equation for the total thermal conductance for a bi-material thermal detector is given by [10]:

$$G = G_{leg} + G_{rad} + (G_{air,conv} + G_{air,cond})$$ (2.3)

Since the device is typically operated under low pressure in a vacuum cell, the convective ($G_{air,conv}$) and conductive ($G_{air,cond}$) thermal conductance due to air are negligible. The total thermal conductance can therefore be expressed as:

$$G = G_{leg} + G_{rad}$$ (2.4)

G_{leg} is the thermal conductance through the legs to the heat sink and G_{rad} is the thermal conductance due to radiation emitted from the surface of the pixel. In general, G_{rad} is relatively small compared to G_{leg}. The value of G_{rad} is given by [11]:

$$G_{rad} = 4A\sigma T^3 (\varepsilon_{Al} + \varepsilon_{SiO_2})$$ (2.5)

where A is the total surface area of the detector, σ is the Stephan-Boltzmann constant, T is the working temperature of the detector, and ε_{Al} and ε_{SiO_2} are the emissivities of Al and SiO_2, respectively.

The general equation for G_{leg} is given by [3]:

$$G_{leg} = \frac{g \cdot W \cdot t}{l}$$ (2.6)

where g is the thermal conductivity of the material , W is the width of the leg, t is the total thickness of the leg and l is the total length of the legs.

The equation for the legs composed of Al and SiO_2 layers is thus given by:

$$G_{Al+SiO_2} = \frac{g_{Al} \cdot W \cdot t_{Al}}{l_{Al+SiO_2}} + \frac{g_{SiO_2} \cdot W \cdot t_{SiO_2}}{l_{Al+SiO_2}}$$ (2.7)

Since the g_{Al} is much bigger than g_{SiO_2}, the second term can be ignored. The equation becomes:

$$G_{Al+SiO_2} \approx \frac{g_{Al} \cdot W \cdot t_{Al}}{l_{Al+SiO_2}} \qquad (2.8)$$

The equation for the legs with only SiO₂ layer is given by:

$$G_{SiO_2} = \frac{g_{SiO_2} \cdot W \cdot t_{SiO_2}}{l_{SiO_2}} \qquad (2.9)$$

The G_{leg} for combining two parallel components in 2.8 and 2.9 can be expressed as:

$$\frac{1}{G_{leg}} = \frac{1}{G_{Al+SiO_2}} + \frac{1}{G_{SiO_2}} \qquad (2.10)$$

The total G_{leg} for symmetric legs on both sides will be:

$$G_{leg} = 2W \left(\frac{g_{Al} t_{Al} g_{SiO_2} t_{SiO_2}}{l_{Al+SiO_2} g_{SiO_2} t_{SiO_2} + l_{SiO_2} g_{Al} t_{Al}} \right) \qquad (2.11)$$

Again, since the g_{Al} is much bigger than g_{SiO_2}, ignoring the $l_{Al+SiO_2} g_{SiO_2} t_{SiO_2}$ term, Equation 2.11 becomes:

$$G_{leg} \approx 2 \times \frac{W g_{SiO_2} t_{SiO_2}}{l_{SiO_2}} \qquad (2.12)$$

Substituting the values of $g_{SiO_2} = 1.4 (Wm^{-1}K^{-1})$, $W = 8\mu m$, $l_{SiO_2} = 282\mu m$ from Table 1 and Table 2 into Equation 2.7 will result in $G_{leg} = 3.97 \times 10^{-2} t_{leg} (WK^{-1})$.

From Equation 2.5, the G$_{rad}$ can be calculated by using $A = 1.76 \times 10^{-8} (m^2)$, assuming the thermal radiation is only emitted from the absorber while the surface area of the legs is too small to be negligible, $\sigma = 5.67 \times 10^{-8} (W^{-2}K^{-4})$, $T = 300K$, ε_{Al} and ε_{SiO_2} is 0.02 and 0.08 respectively gives $G_{rad} = 8.84 \times 10^{-8} (WK^{-1})$.

11

Having a fixed value for the width and the length of the legs, G_{leg} can be changed by varying the leg thickness. The value of G_{rad} depends only on the surface area of the pixel, which is nearly independent of the thickness of the legs. Thus, for a fixed pixel area, the G_{rad} remains constant while the G_{leg} decreases with its thickness. Therefore, the minimum value of thickness to reduce the overall thermal conductance can be obtained when G_{leg} is equal to G_{rad} as illustrated in Figure 8.

However, due to the issues of stress differential resulting from the micofabrication process, $700\,\mu m$ is the lowest value of thickness of SiO_2 that has been used in these calculations.
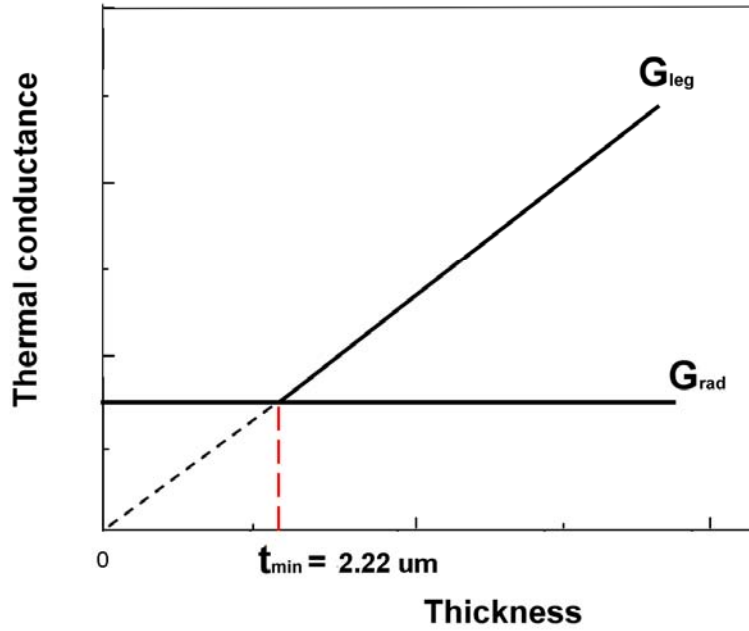

Figure 8.   Thermal conductance as a function of leg thickness

III.   FINITE ELEMENT SIMULATION

The response of the pixel for absorbed THz power is simulated using COMSOL finite element simulator. In the model, the top reflector material was temporarily removed in order to eliminate the stress effects in the central region of the pixel. In addition, the exact material to be used for both absorption of THz radiation and reflection of the readout is a subject of a separate research project. The value of incoming power in this simulation was estimated based on a previous experiment where $1\,mW$ incident power was illuminated on $120{\times}160$ pixel infrared FPA with $50\,\mu m \times 50\,\mu m$ per pixel area. This corresponds to an intensity of incident power of about $20.8\,Wm^{-2}$ and in COMSOL simulation, 100% absorption is assumed.

It is important to determine the resonance frequencies of the entire structure since it can affect the speed of operation of the pixels under time varying THz power. If the lowest resonance frequency is close to the frequency of the time varying THz signal, a non-linear response can result from the sensor. On the other hand, higher resonance frequencies are associated with stiffer spring constant resulting in smaller deflection of the cantilever. Figure 9 shows the first three eigen modes simulated using COMSOL of the pixel structure shown in Figure 7. The first mode is the most important in the design of the pixel.

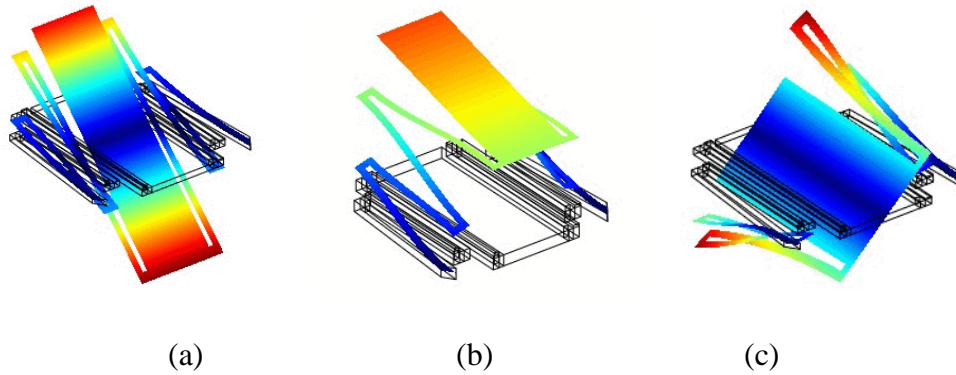(a)   (b)   (c)

Figure 9.   The lowest three eigen modes (a) 4921 Hz, (b) 5707 Hz and (c) 15104 Hz

The frequency response of a resonance is usually not be exactly symmetric about the resonant frequency. The amplitude of the oscillations x for a damped oscillator can be expressed as:
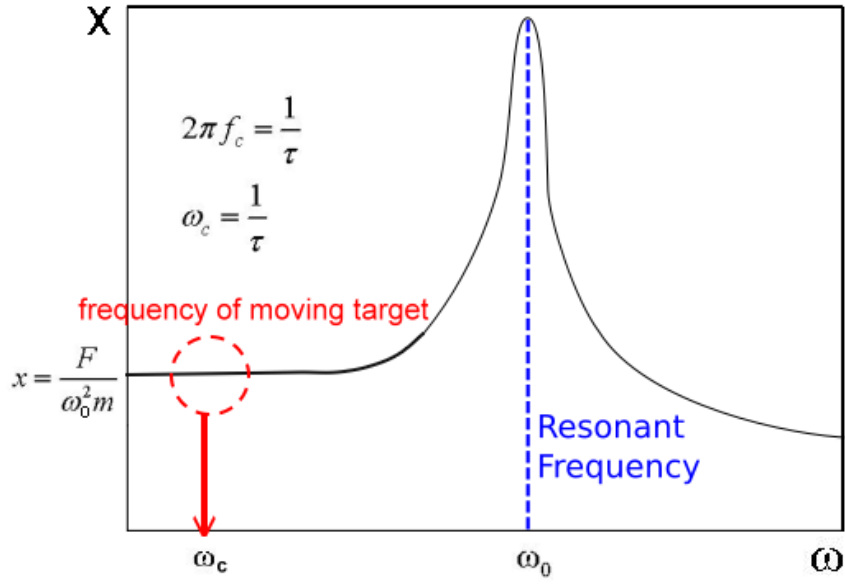
$$x = \frac{F/m}{\sqrt{(\omega_0^2 - \omega^2)^2 + (\gamma\omega)^2}}$$ (3.1)

where F is the driving force, m is the mass, ω is the driving frequency, ω_0 is the resonant frequency and γ is the ratio of damping coefficient b to the mass m. A typical resonant curve is shown in Figure 10 (a). When the resonant frequency is much larger than the driving frequency (i.e., $\omega \ll \omega_0$), the equation can be simplified as:
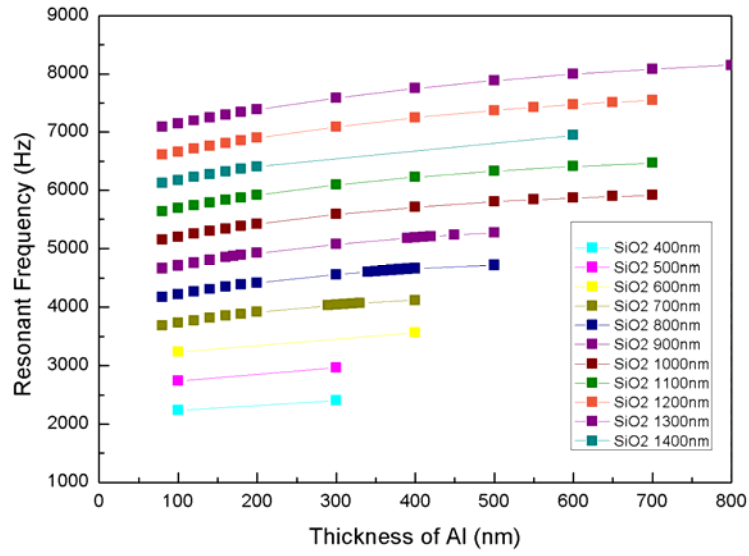
$$x \approx \frac{F/m}{\omega_0^2} = \frac{F/m}{k/m} = \frac{F}{k}$$ (3.2)

which shows that the response amplitude is proportional to the driving force, $F = kx$, where k is the spring constant. Under this condition, the amplitude of oscillations is independent of the driving frequency and proportional to the driving force providing a linear response.

In the design, the first mode for different leg thicknesses was simulated and graphed in Figure 10(b). It was found that the lowest resonant frequency was 2000 Hz. This result is far from the speed of operation of the pixels (30 Hz) needed for real-time imaging. It is known that a frequency of 30 Hz is the minimum speed for a human eye to decipher a motion picture. The thickness in the simulation will present a steady condition for the amplitude response.

(a)

(b)

Figure 10.   (a) Amplitude as a function of frequency for a damped oscillator and (b) resonant frequency of a pixel as a function of leg thickness

15

A.   MAXIMUM BENDING

As shown in Figure 11, the total displacement of the cantilever in the z-direction can be calculated by summing the displacement at points 1 and 2. The sine of the deflection angle (θ) is trigonometrically equal to the total displacement in the vertical direction divided by the length of the pixel. For small θ, $\sin\theta \sim \theta$ and the deflection angle are equal to the vertical displacement.
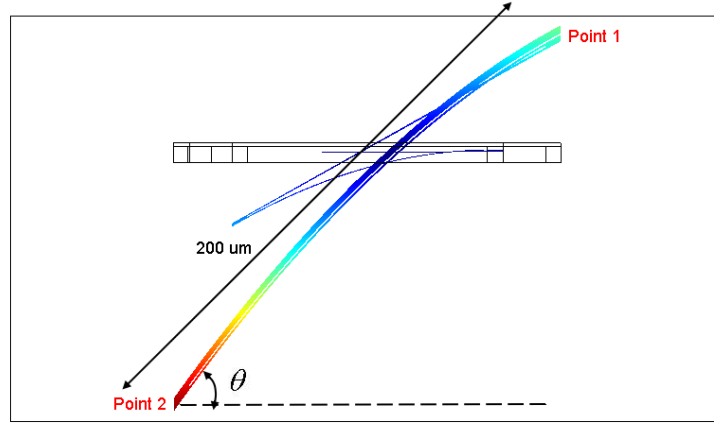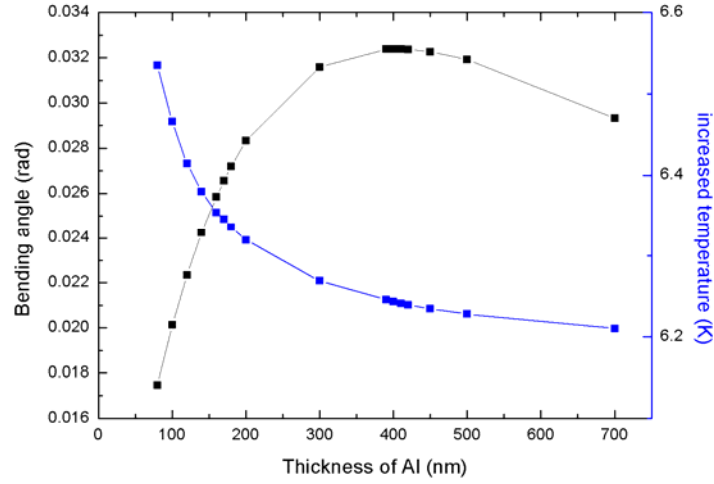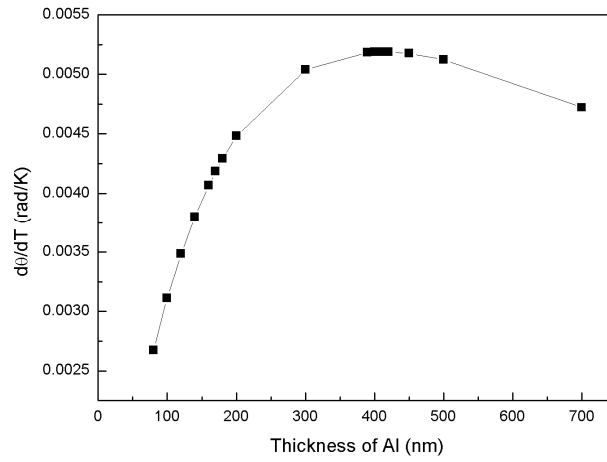

Figure 11.   Determination of angle of deflection

By measuring the temperature increase in the absorber (the temperature difference between heat sink and absorber), $\dfrac{d\theta}{dT}$ can be calculated for different leg thicknesses. Aluminum has a higher thermal expansion coefficient than silicon dioxide and, thus, increasing the thickness of the Al will increase the bending angle as shown in Figure 12 (a). However, it was found that for Al thickness above 400 nm (see Figure 12 (a)), the bending angle starts to decrease. This is primarily due to reduction in temperature rise of the pixel as the aluminum thickness is increased as a result of higher thermal conductance of the legs. The smaller temperature increase incurs a smaller deflection. The value of $\dfrac{d\theta}{dT}$ then can be simply obtained by dividing one by the other, as shown in Figure 12 (b).

16

The $\dfrac{d\theta}{dT}$ curve is almost identical to the bending angle curve. As the author fixed the thickness of Al and varied SiO$_2$, the $\dfrac{d\theta}{dT}$ curve had the same behavior.

(a)

(b)

Figure 12.　(a) Deflection angle and change in pixel temperature as a function of Al thickness with 900 nm SiO$_2$, (b) dependence of $\dfrac{d\theta}{dT}$ as a function of Al thickness with 900 nm SiO$_2$

17

The 3D graph in Figure 13 shows the tendency of the $\dfrac{d\theta}{dT}$ curve by varying both aluminum and silicon dioxide thicknesses. The data in Figure 13 can be used for determining the optimum parameters for achieving the highest rate of deflection with temperature.
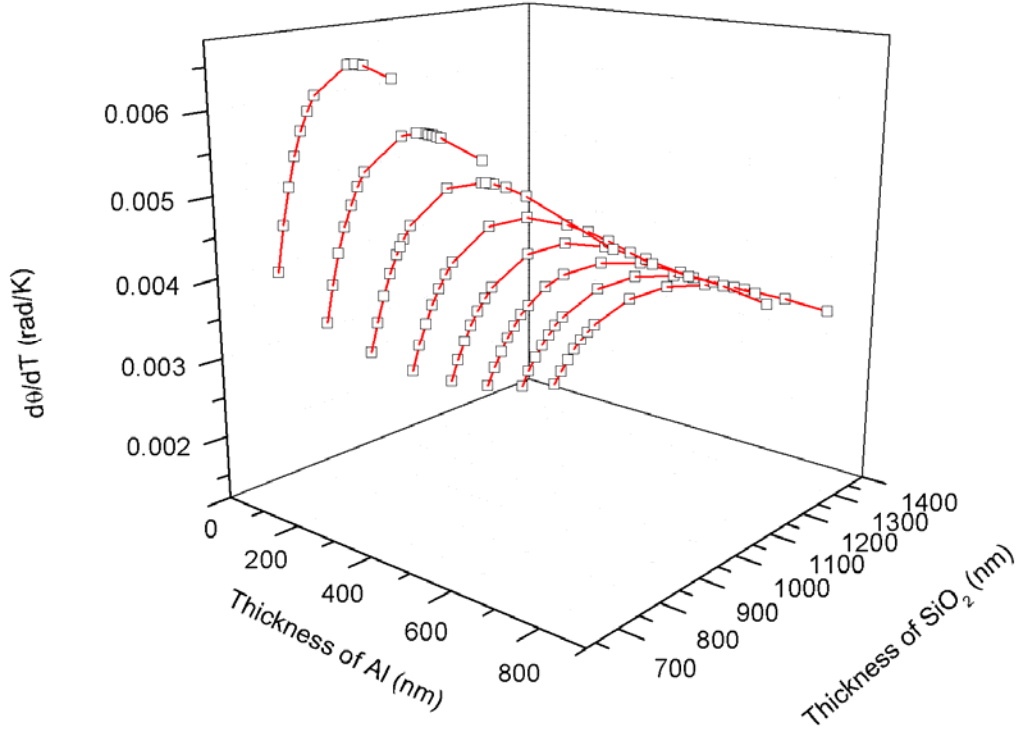

Figure 13.   3D graph of the $\dfrac{d\theta}{dT}$ by varying the thicknesses of both SiO$_2$ and Al

B.   RESPONSE TIME

In order to evaluate the time constant τ, Equations 2.2 and 2.6 can be used along with the heat capacity of the absorber (200 x 88 μm) and thermal conductance. By assuming the mass of the Al layer is too small to be negligible, the heat capacity of the structure can be calculated by the specific heat capacity of SiO$_2$ multiplied by the mass of SiO$_2$ obtained from COMSOL, $C\,(JK^{-1}) = 730\,(JKg^{-1}K^{-1}) \times mass\,(Kg)$, which means the

18

heat capacity is directly proportional to the total thickness of the SiO_2 layer since the pixel area is a constant. As mentioned in Chapter II, the thermal conductance is proportional to the thickness of SiO_2 and Al. As a result, by fixing the thickness of the SiO_2 layer and increasing the thickness of the Al layer, the time constant τ decreased as shown in Figure 14. However, fixing the thickness of the Al layer and increasing the thickness of the SiO_2 layer, the time constant τ increased. This indicates that the heat capacity dominates the thermal conductance in optimizing the response time.

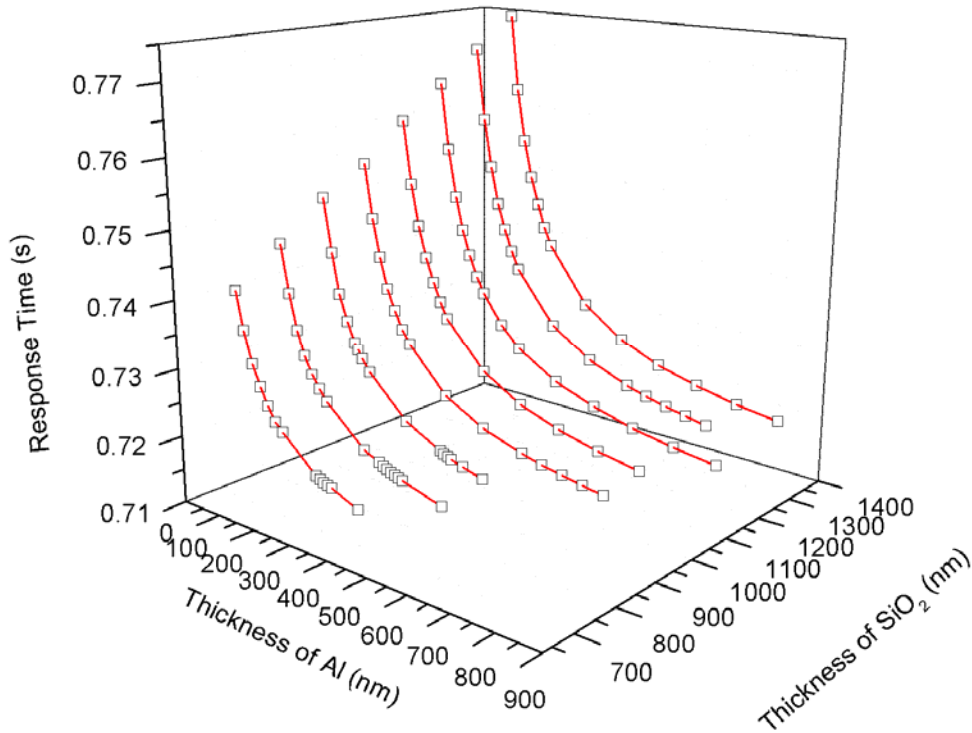

Figure 14.   3D graph of the response time by varying the Al and SiO_2 thicknesses

C.   QUALITY FACTOR

The quality factor, Q is necessary in the calculation of the Noise Equivalent Temperature Difference (NETD). The details of the NETD and its computation will be discussed in the next section. Q-factor of a resonator is generally defined as the ratio of

the maximum energy stored to the energy lost in a single oscillation. Therefore, devices with higher quality factors will have larger stored energy when driven at the resonant frequency.

Q factor also represents the sharpness of the resonance curve shown in Figure 16. A high quality factor is characterized with a high response peak and a narrow bandwidth, which is the frequency difference between the points of amplitude at $\frac{1}{\sqrt{2}}$ (also known as 3dB) of the peak, as shown in Figure 15 [12].
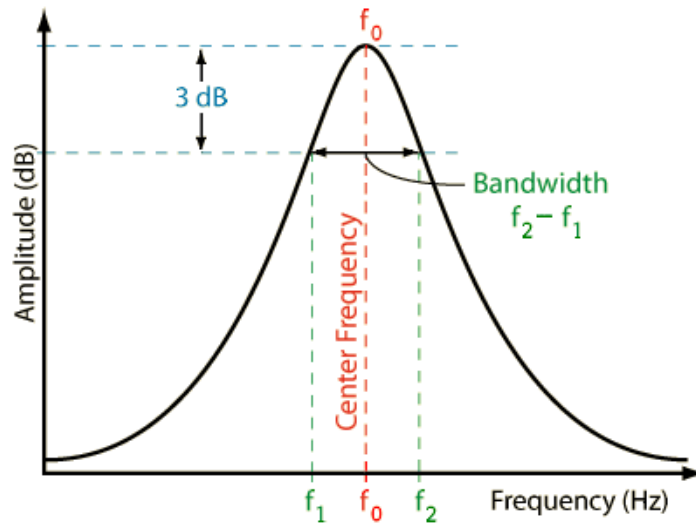

Figure 15.   Bandwidth of resonant frequency (From [12])

Quality factor can be expressed as:

$$Q = \frac{energy\ stored\ per\ cycle}{energy\ dissipated\ per\ cycle} = \frac{resonant\ frequency}{bandwidth\ at\ \frac{1}{\sqrt{2}}\ of\ peak} \tag{3.3}$$

The damping constant ($C_{damping}$) due to the motion of a cantilever in air can be estimated using [13]:

$$C_{damping} = cantilever\ width \cdot \pi\sqrt{b\rho\omega\mu} \tag{3.4}$$

20

where ω is the vibration frequency, ρ is the fluid density, and μ is the fluid viscosity, b is a constant number dependant on the structure design. In air, the density is $\rho = 1.025\ kg \cdot m^{-3}$ and viscosity is $\mu = 1.871 \times 10^{-5} Pa \cdot s$.

Equation 3.4 was based on a cantilever with rectangular cross-section moving in the air where the parameter b is approximately equal to 2. Considering the multi-leg design of the structure, a higher damping and hence a higher value of b is expected. The increase in b is due to the increase in the perimeter of the structure resulting in increased air damping as it vibrates. The value of b is usually estimated by measuring the bandwidth of the resonance peak experimentally. Figure 16 shows the experimental setup used for measuring amplitude as a function of driving frequency using a laser vibrometer. A speaker was used as a sound source, providing an acoustic plane wave in the 100 to 7000 Hz frequency range. In the measurement, a single pixel of a FPAs fabricated is employed with laser light from the vibrometer, focused using a microscope objective lens assembly.
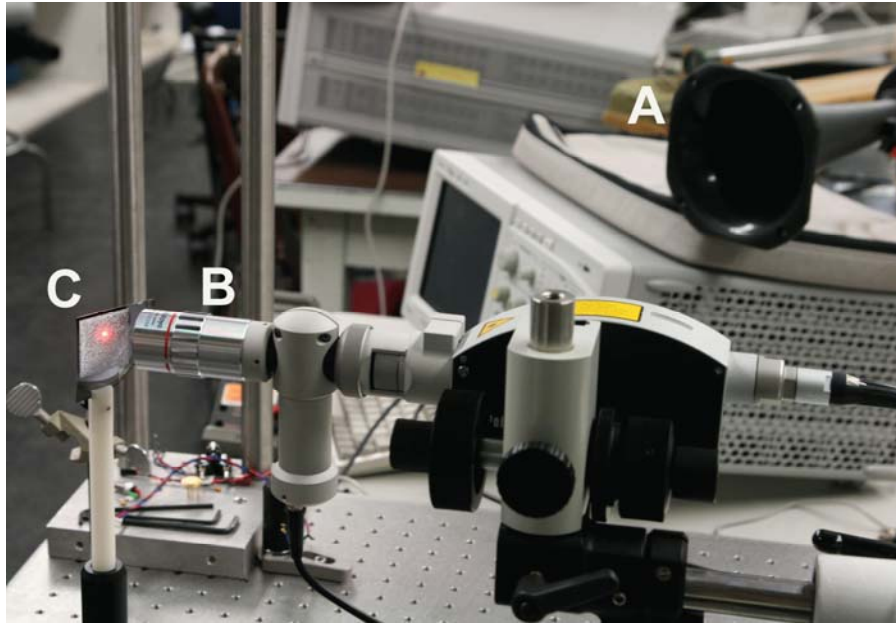

Figure 16.   Lab setup for measuring frequency response of a pixel. (A) Speaker for sound source with directional cone. (B) Laser vibrometer with a microscope objective lens. (C) FPAs

As seen in Figure 16, the measured frequency of a pixel is compared with the simulation with b = 3 and without residual stress (green line), showing a higher resonant frequency and a symmetric peak. However, a residual stress of $10^7 Pa$ on Al and $3 \times 10^8 Pa$ on SiO$_2$ was found to exist by the characterization of thin films performed during the microfabrication process. Inclusion of the stresses in the simulation resulted in decrease of the resonant frequency; the curve became asymmetric (blue line in Figure 17), which is closer to the experimental data but with a relatively wide bandwidth. The red line in Figure 17 is the simulated data with b = 2 and stresses that show a close agreement with the measurements.
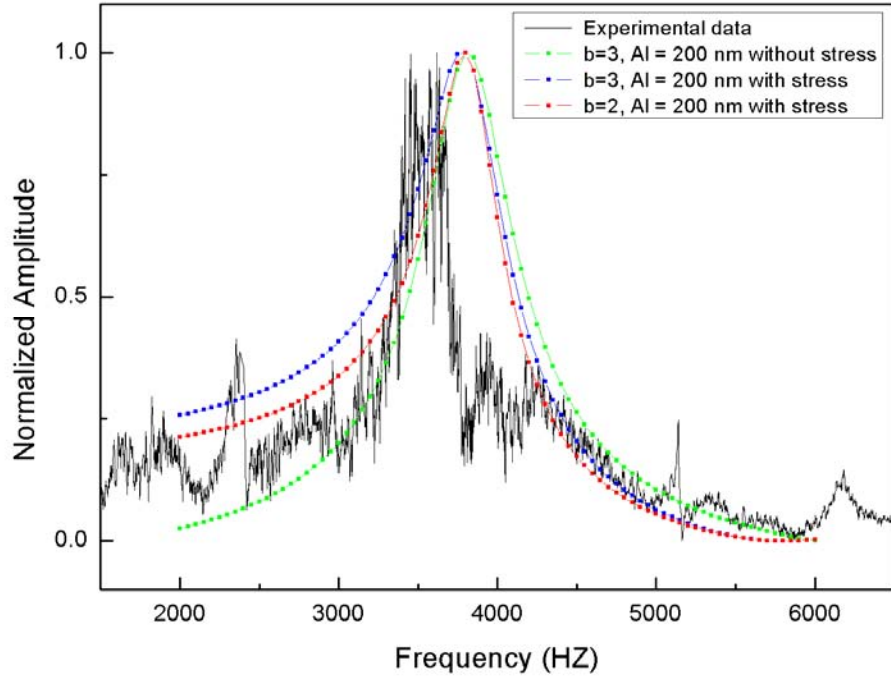

Figure 17.   Comparison of simulated frequency response with experimental data

By using Equation 3.4 with b = 2, the frequency response is simulated for a set of pixels with different layer thickness parameters; the results are shown in Figure 18. The value of the Q factor can be calculated by Equation 3.3 and ranges from 20 to 45. These

22

values are then used to calculate the Noise Equivalent Temperature Difference (NETD) performance of the detector in the FPAs for the next section. Note that the Q factor in operating condition (vacuum) will be higher.
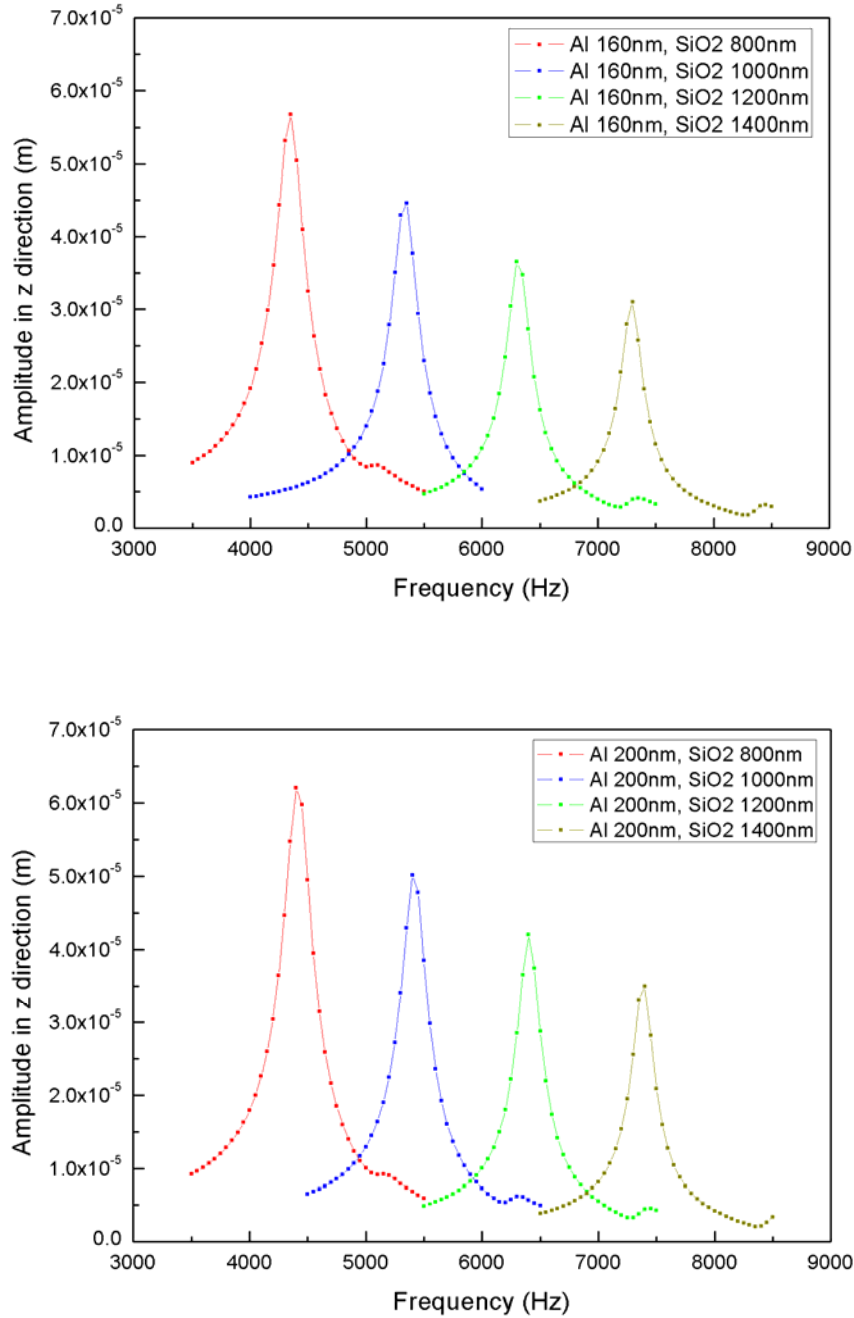

Figure 18.   Frequency responses of pixels with Al thickness from 160 nm to 200 nm and SiO$_2$ thickness from 800 nm to 1400 nm

23

D. NOISE EQUIVALENT TEMPERATURE DIFFERENCE

Noise Equivalent Temperature Difference (NETD) of a sensor is defined as the amount of temperature of a target above the background needed to produce a signal-to-noise ratio equal to 1 at the sensor. Both the target and background are assumed to be blackbody sources. An equation of NETD can be expressed as [3].

$$NETD_N = \frac{Zn}{\triangle Z} \tag{3.5}$$

where Zn is the amplitude of noise and $\triangle Z$ is the amplitude of signal. For the micro-cantilever, the signal will be the deflection of the device as a result of power from the target, which can be expressed as [3]:

$$\triangle Z = \tau_0 \frac{A}{4F^2} R(w)(\frac{dP}{dT})_{\lambda_1 - \lambda_2} T \tag{3.6}$$

where A is the surface area of a pixel, F is the f-number of the lens used for focusing the radiation beam onto the detector, and τ_0 is the transmission of the lens. In the case of THz detection, the lens is made of polyethylene. The average transmission of the lens in the THz region (1-5 THz) is about 0.77, as shown in Figure 19 [14].
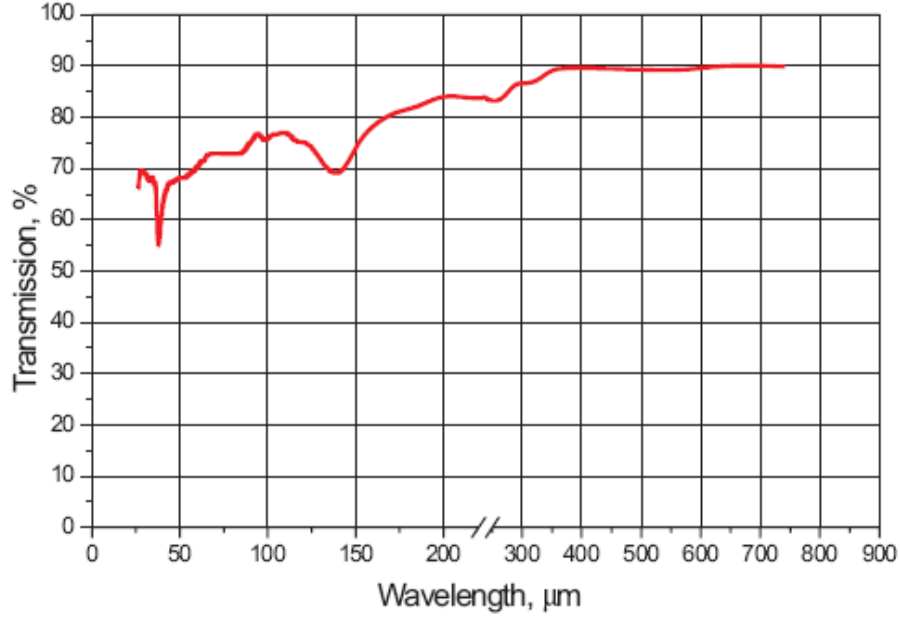
Figure 19.   Transmission of 2 mm-thick high density polyethylene in THz region (From [14])

$R(w)$ is the responsivity of the sensor, T is the room temperature and $(\dfrac{dP}{dT})_{\lambda_1 - \lambda_2}$ is the slope of the black body radiation curve from λ_1 to λ_2. For the desired frequency range, 1-5 THz, $(\dfrac{dP}{dT})_{\lambda_1 - \lambda_2}$ can be obtained by approximating the power emitted by a black body source in THz spectral range as [2]:

$$P(T) \approx \int_0^{v} \frac{2\pi kT}{c^2} v^2 dv \approx \frac{2\pi kT}{3c^2} v_c^3 \qquad (3.7)$$

where v_c is the upper limit of frequency range and the lower limit is assumed to be 0. By taking the derivative with respect to T on both sides, the equation becomes:

$$(\frac{dP}{dT}) = \frac{2\pi k}{3c^2} v_c^3 \qquad (3.8)$$

25

Using cutoff frequency $v_c = 5\text{THz}$ and calculating $(\dfrac{dP}{dT})$ from Equation 3.8 gives a value of 0.06.

The primary source of micro-cantilever noise comes from the temperature fluctuations. The root mean square (average) of this noise can be expressed as [3]:

$$< Z_{TF}^2 >^{1/2} = \frac{R(\omega)T\sqrt{4k_B BG}}{\eta}$$
(3.9)

Where k_B is the Boltzmann constant of $1.38\times10^{-23}m^2kgs^{-2}K^{-1}$, B is the frequency bandwidth of the sensor—which is limited by the thermal time constant ($\sim 30Hz$)—G is the thermal conductance of the sensor and η is the absorbance ($\sim$0.3) for a typical THz absorbing material used in sensor fabrication.

Additional noise is introduced from the lattice vibrations due to the thermal energy (k_BT), which excite some of the resonant modes. This additional vibration is called thermo-mechanical noise and is expressed as [3, 15]:

$$< Z_{TM}^2 >^{1/2} = \sqrt{\frac{4k_B TB}{Qk} \frac{\omega_0^3}{(\omega_0^2 - \omega^2)^2 + \dfrac{\omega^2\omega_0^2}{Q^2}}}$$
(3.10)

Notice that the operating frequency ω in this case is much smaller than the resonant frequency ω_0; therefore Equation (3.10) can be simplified as:

$$< Z_{TM}^2 >^{1/2} = \sqrt{\frac{4k_B TB}{Qk\omega_0}}$$
(3.11)

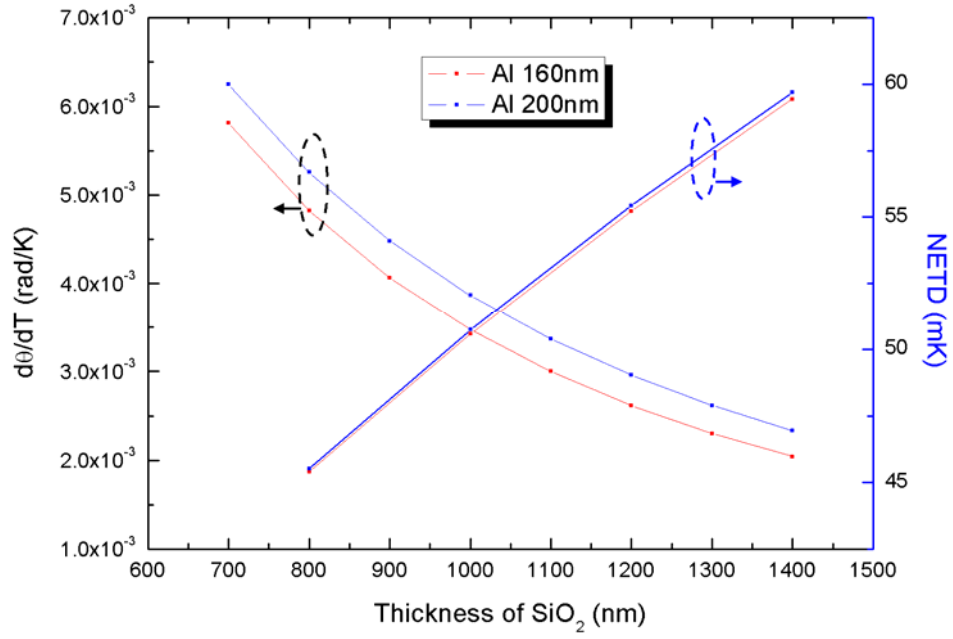where Q is the quality factor and k is the spring constant.

26

By the definition of NETD (Equation 3.5), the $NETD_{TF}$ (due to temperature fluctuations) and the $NETD_{TM}$ (due to thermal mechanical noise) then can be obtained by combining Equation (3.9) with (3.10) and Equation (3.9) with (3.11):

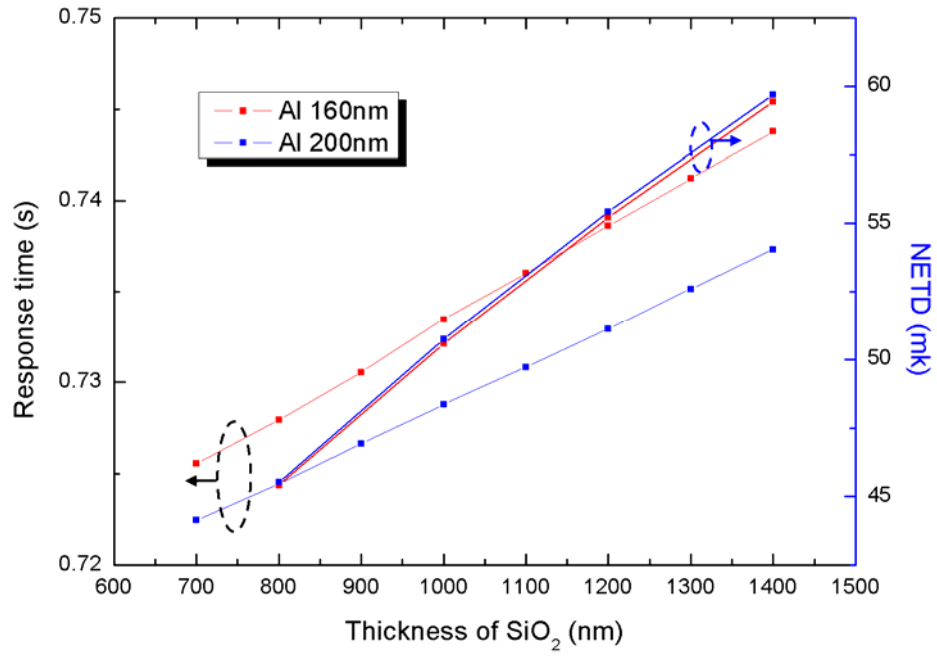$$NETD_{TF} = \frac{4F^2 T \sqrt{4K_B BG}}{\tau_0 \eta A (\frac{dP}{dT})_{\lambda_1 \sim \lambda_2}} \tag{3.12}$$

$$NETD_{TM} = \frac{4F^2}{\tau_0 AR(\omega)(\frac{dP}{dT})_{\lambda_1 \sim \lambda_2}} \sqrt{\frac{4k_B TB}{Qk\omega_0}} \tag{3.13}$$

The total value of NETD thus can be evaluated by taking a square root of the sum of the squares of individual NETDs.

The graphs of NETD with $\frac{d\theta}{dT}$ and NETD with response time are shown in Figures 20 (a) and (b), respectively. As displayed in the graph, when the thickness of Al is increased, the value of NETD increases slowly at about 0.02 mK per 50 nm. When the thickness of SiO_2 increased, the value of NETD increased rapidly at about 2 mK per 50 nm.

(a)

(b)

Figure 20.　　(a) NETD with $\dfrac{d\theta}{dT}$　(b) NETD with response time

28

IV.   ANALYSIS OF RESULTS

A.   SELECTION OF THICKNESS

It is important to select the most favorable thickness combination of the bi-material detector in order to achieve the optimal performance. The challenging part comes from the need to simultaneously optimize all the desirable parameters such as sensitivity, response time and noise. As shown in the equations above, these complex physical properties have adverse effects on each other. Therefore, optimizing one often worsens another.

One way to simplify this problem is to create a simulation of numerous values of different thickness settings and then graph the results. The desired properties of unsimulated data can be predicted from the resultant curve. From previous chapters, the 3D graph in Figure 14 shows that the response time will decrease by either reducing the thickness of SiO_2 or increasing the thickness of Al. The maximum value of $\dfrac{d\theta}{dT}$ can be found in each curve from the 3D graph on Figure 13, which was simulated by 100 nm intervals of the SiO_2 layer thickness. The peak point with the highest deflection amplitude and the smallest total thickness with the smallest response time from Figure 21 will provide the best solution. In conjunction with these selection criteria, the least total thickness that can be considered must be 700 nm due to restrictions on current fabrication techniques. As discussed previously, the value of NETD of all the combinations with SiO_2 thicknesses less than 1400nm will never be higher than 62 mk, which is relatively low for uncooled thermal sensors in the THz spectrum.
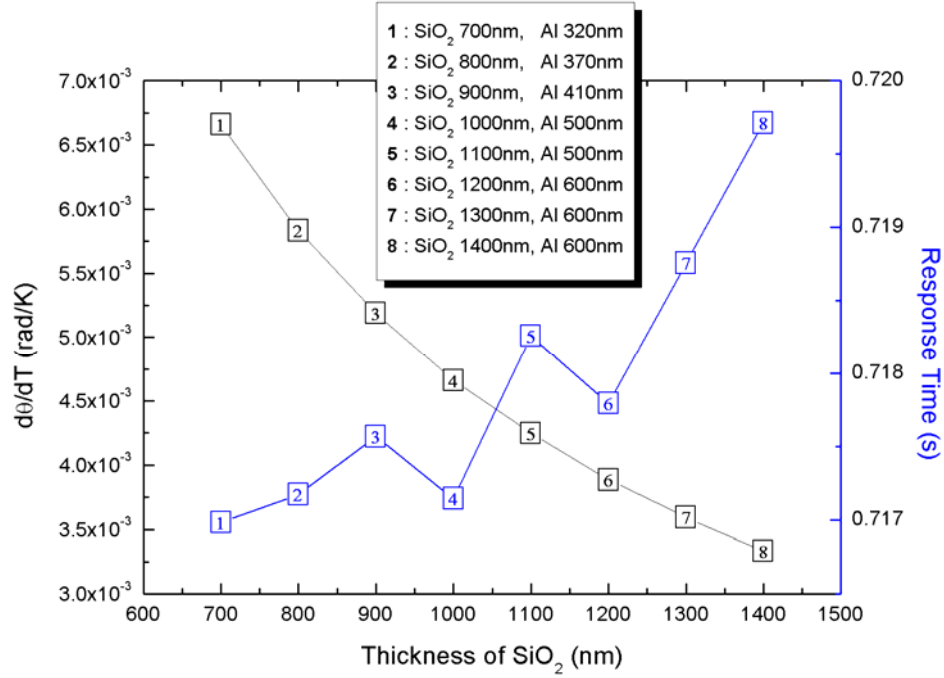
Figure 21.   Response time and peak deflection rate as a function of SiO$_2$ thickness

Another method for determining the combination of thicknesses is to fix one or two variables and vary the remaining parameters. For example, in Figure 22, if the desired NETD must be lower than that of the thickness combination of 4 (SiO$_2$ 800 nm, Al 200 nm), which is 46 mK, and the response time has to be lower than thickness combination 1 (SiO$_2$ 800nm, Al 80nm), which has a value of 0.75 second, this will limit the choice of bending angles of combinations 2 and 3. The combination of 3 will thus be selected because it provides the maximum angle.
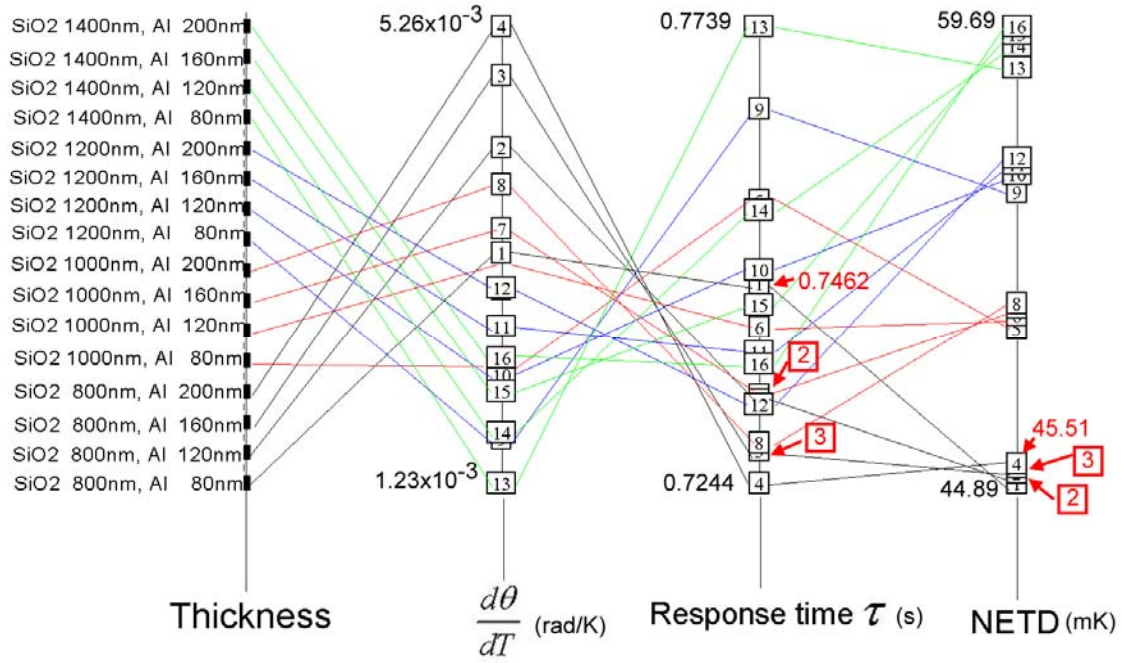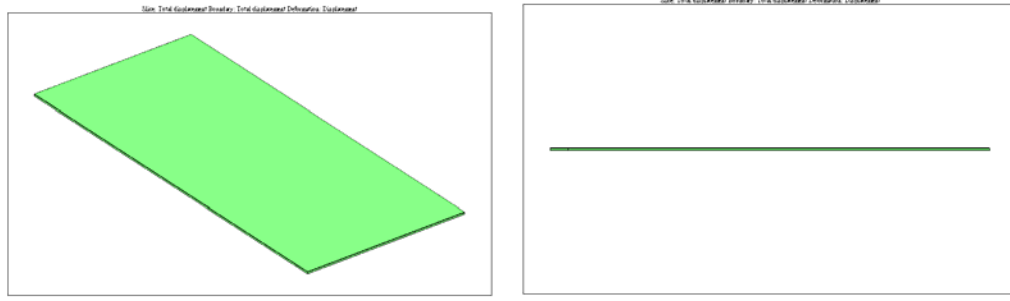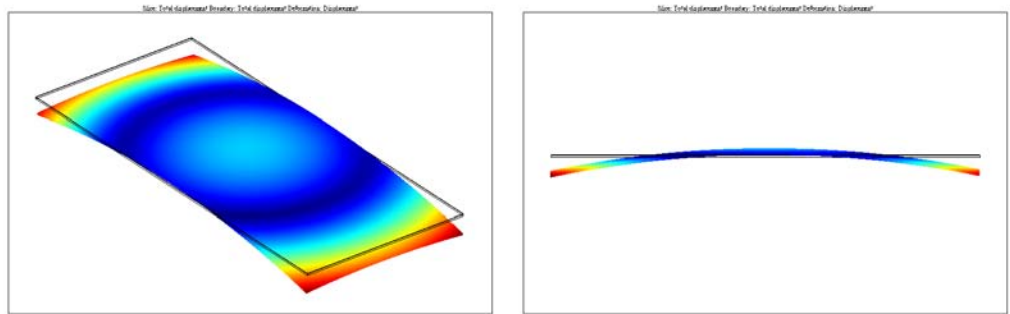
Figure 22.   Thickness sets with the optimized desirable parameters

B.   THE EFFECT OF STRESS FORCE

Another important physical effect on the performance of bi-material cantilevers is the initial deflection due to the residual stress in the two materials. This stress builds up during the chemical deposition stage of the micro-fabrication process [16, 17]. The residual stress is a result of a difference in the shrinking rate between two materials in the x-direction and y-direction when cooled down.   These effects form a curvature as shown in Figure 23.

(a)

(b)

Figure 23.   Top and side views of (a) structure without residual stress and (b) structure with residual stress

The initial curvature highly affects the optical readout caused by thermal deflection due to THz absorption.   These factors are important for consideration in performance analysis in order to properly choose the realistic thicknesses for simulation.

V.   CONCLUSION

This thesis has successfully demonstrated the use of COMSOL multi physics finite element simulation with heat transfer and solid stress models for the design of a bi-material cantilever sensor in the THz region. The results for changing thicknesses and the physical effect on the sensitivity, response time and noise were reported. From these results, the best combination will be compared experimentally to the proposed device. The characterization methods developed in this study laid a foundational process for a more advanced structure design and more complex simulations. In the future, coupling these results with the COMSOL RF model could enable a simulated heat generation source from THz radiation to more closely emulate the actual device.

THIS PAGE INTENTIONALLY LEFT BLANK

LIST OF REFERENCES

[1]   L. L. Li, W. Xua, Z. Zeng, A. R. Wright, C. Zhang, J. Zhang, Y. L. Shi, and T. C. Lu, *Terahertz band-gap in InAs/GaSb type-II superlattices*, China, July 2008.

[2]   B. N. Behnken, "Real-time terahertz imaging using a quantum cascade laser and uncooled microbolometer focal plane array," Monterey, March 2008.

[3]   D. Grbovic, "Imaging by detection of infrared photons using arrays of uncooled micromechanical detectors," The University of Tennessee Knoxville, May 2008.

[4]   D. Grbovic and G. Karunasiri, "Fabrication of bi-material MEMS detector arrays for THz imaging," Department of Physics, Naval Postgraduate School, Monterey.

[5]   Web site, "Electro optical Industries," http://www.electro-optical.com/html/bb_rad/emissivity/matlemisivty.asp, last accessed 7 November 2009.

[6]   Z. Guoa et al., "Performance analysis of microcantilever arrays for optical readout uncooled infrared imaging," *ScienceDirect*, February 2007.

[7]   F. Dong et al., "An uncooled optically readable infrared imaging detector. Sensors and actuators," *Physical*, 133(1): p. 236–242, 2007.

[8]   L. R. Senesac et al., "IR imaging using uncooled microcantilever detectors," *Ultramicroscopy*, 97: p. 451, 2003.

[9]   Web site, "The MultiMEMS MPW Process," http://it-assistant.eu/mbcd/sensonor_3.html, last accessed 7 November 2009.

[10]   S. Shi et al., "Design, simulation and validation of a novel uncooled infrared focal plane array," *ScienceDirect*, May 2006.

[11]   P. G. Datskos and N. V. Lavrik, "Detectors—Figures of Merit," in *Encyclopedia of Optical Engineering*, 2003.

[12]   Web site, "Tontechnik-Rechner," http://www.sengpielaudio.com/calculator-bandwidth.htm, last accessed 5 October 2009.

[13]   W. Zhang et al., "Frequency dependent fluid damping of micro/nano flexural resonators: Experiment, model and analysis," *ScienceDirect*, 4 June 2006.

[14]   Web site, "Tydex," http://www.tydexoptics.com, last accessed 7 November 2009.

[15]   D. Sarid, *Scanning Force Microscopy*, New York: Oxford University Press, 1991.

[16]   Z. Cao and X. Zhang, "Experiments and theory of thermally-induced stress relaxation in amorphous dielectric films for MEMS and IC applications," *ScienceDirect*, 8 August 2005.

[17]   Z. Cao and X. Zhang, "Nanoindentation stress–strain curves of plasma-enhanced chemical vapor deposited silicon oxide thin films," *ScienceDirect*, 13 September 2007.

INITIAL DISTRIBUTION LIST

1. Defense Technical Information Center
    Ft. Belvoir, Virginia

2. Dudley Knox Library
    Naval Postgraduate School
    Monterey, California

3. Gamani Karunasiri
    Naval Postgraduate School
    Monterey, California

4. Dragoslav Grbovic
    Naval Postgraduate School
    Monterey, California

5. Poyuan Liao
    Chung-Cheng Institute of Technology
    Taiwan